Constitutive modeling and systematic evaluation of asphalt concrete's viscoelastic tension-compression asymmetry effect on pavement performance

Zhifei Tan[a,b], Hui Li [a,b,c], Zhen Leng[a,b*], Denis Jelagin[d*], Peng Cao[e], Cong Du[f], Binbin Yin[a,b]

[a]Department of Civil and Environmental Engineering, The Hong Kong Polytechnic University, Hong Kong, China

[b]Research Center for Resources Engineering Towards Carbon Neutrality, The Hong Kong Polytechnic University, Hong Kong, China

[c]School of Transportation, Southeast University, Nanjing, 211189, China

[d]Department of Civil and Architectural Engineering, KTH Royal Institute of Technology, Brinellvägen 23, 10044, Stockholm, Sweden

[e]Faculty of Architecture, Civil and Transportation Engineering, Beijing University of Technology, Beijing 100081, China

[f]School of Qilu Transportation, Shandong University, Jinan 250002, Shandong Province, China

Corresponding Authors[*]

Zhen Leng, Email: zhen.leng@polyu.edu.hk

Denis Jelagin, Email: denis.jelagin@abe.kth.se

Abstract

Asphalt concrete (AC) exhibits significant tension-compression (TC) asymmetry, which is currently not considered in pavement design. This study develops a novel temperature-dependent dual viscoelastic model to quantitatively capture the viscoelastic behavior of AC. Unlike the conventional viscoelastic constitutive model, the proposed model decomposes strain into tensile and compressive components to characterize AC's TC asymmetry. Additionally, a systematic modeling framework with intrinsic TC asymmetry is developed for the first time to predict the response of pavement under moving tire load. The results illustrate that implementing the proposed dual viscoelastic model enlarges both the vertical deformation of pavements and the tensile and shear strains in the AC layers, bringing it closer to the realistic scenario compared to the conventional model that only considers compression properties. Furthermore, high temperatures and low vehicular speeds exacerbate the substantial effects of AC's TC asymmetry on asphalt pavement. This study provides a valuable method to capture AC's TC asymmetry and predict pavement response more accurately, giving better insight into pavement response and enhancing pavement design and maintenance.

Keywords: Asphalt pavement, Tension-compression asymmetry, Constitutive modeling, Numerical modeling

1. Introduction

Asphalt concrete (AC) is a particulate-filled material composed of asphalt binder, aggregates, and air voids, widely used in pavement construction (Leng *et al.* 2019, 2021, Cao *et al.* 2020, Zou *et al.* 2024). Given its high heterogeneity, AC exhibits intricate mechanical performance under traffic loads and climatic conditions (Darabi *et al.* 2011, Cao *et al.* 2017, Lu *et al.* 2020, Luo *et al.* 2020). Although AC is generally considered an isotropic linear viscoelastic material at small strain levels (<200 με), significant tension-compression (TC) asymmetry has been observed (Monismith and Secor 1962, Khanal and Mamlouk 1995, Katicha *et al.* 2010, Levenberg 2015, Nguyen *et al.* 2016). The TC asymmetry, or TC nonlinearity, refers to the fact that the mechanical behavior of AC is dependent on load orientation. Generally, the AC mixture is significantly stiffer in compression than in tension (Keshavarzi and Kim 2016, Lv *et al.* 2018, Lytton *et al.* 2018, Dai *et al.* 2021). This stiffening effect in compression has been speculated to be due to the manifestation of the aggregate skeleton (Keshavarzi and Kim 2016, Tan, Jelagin, *et al.* 2023, Cai *et al.* 2024, Tan *et al.* 2024), whereby the high volumetric proportion of the aggregates leads to contact interactions that result in higher compressive stiffness (Sun *et al.* 2017, Cai *et al.* 2020, Zhang *et al.* 2021). A recent study further demonstrated that this asymmetry is caused by the aggregate contact effect (Tan, Yang, *et al.* 2023). It was reported that the microscale asymmetry, induced by aggregate contacts, leads to the remarkable asymmetric behavior of AC at the macroscale level. However, this asymmetry can be weakened at high frequency and low temperature due to the stiffening of the asphalt matrix (Tan *et al.* 2022, Tan, Yang, *et al.* 2023, Li *et al.* 2024), which may explain why AC displays more noticeable TC asymmetry at a longer loading time or higher temperature, as observed experimentally in many previous studies (Lytton *et al.* 2018, Cheng *et al.* 2021). For example, Kallas (1970) measured the dynamic modulus of AC under different loading modes and temperatures, finding that the compressive moduli were insignificant at low temperatures, but more than 50% higher than the tensile moduli when the temperature exceeded 21.1°C.

Two- to five-time differences between the compressive and tensile moduli were observed at intermediate and high temperatures (Cheng *et al.* 2021). Recently, Tan et al. (2023a) conducted a comprehensive evaluation of the dynamic moduli of different AC mixture types through numerical modeling. Their results indicated that open-graded AC mixtures display the highest asymmetry, followed by gap-graded and dense-graded AC mixtures. Consequently, considering the TC asymmetry in the stress analysis of flexible pavements may significantly enhance analysis accuracy.

However, AC's TC asymmetry is rarely accounted for in pavement design. For instance, the mechanistic-empirical pavement design guide (MEPDG) only takes into account the compressive dynamic modulus of AC (Program (NCHRP) 2004). In actual service, asphalt pavements are subjected to complex TC stress and strain due to moving loads (Ahmed *et al.* 2015, Deng *et al.* 2019, Alae *et al.* 2021, Jiang *et al.* 2022). As depicted in Figure 1, the regions behind and in front of the tire experience tension, while the surface asphalt layer below the tire load is under compression. The bottom region, on the other hand, undergoes tension due to bending. Therefore, to accurately capture the pavement response, it is essential to incorporate AC's TC asymmetry.

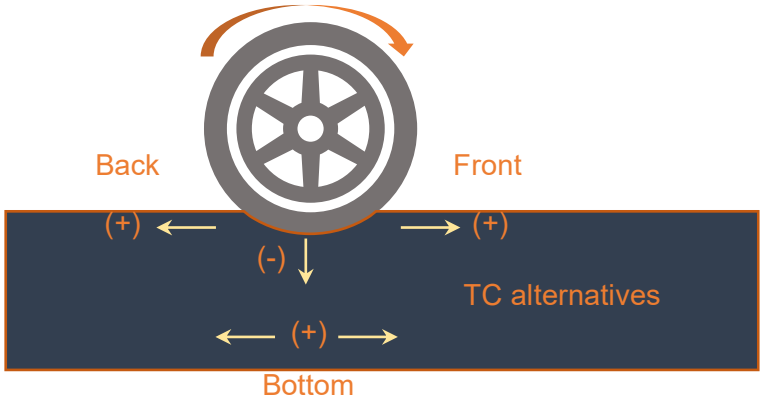

Figure 1 Schematic diagram of asphalt pavement under the moving tire load

Khanal and Mamlouk (1995) applied the compressive and tensile moduli to the top and bottom halves of the AC layer, respectively. A significant reduction in the tensile stress at the bottom layer was observed with respect to the model using the compressive modulus only. However, this simplistic assumption on AC properties cannot represent the complicated TC state in the AC layer. An alternative method to consider the

TC asymmetry of AC is based on bimodular elasticity, which describes the material as having different elastic moduli in T&C. This approach has been extensively researched and applied in composites and biomaterials (Huang *et al.* 2005, Mollica *et al.* 2007, Helmer-Smith *et al.* 2021), and also introduced to pavement modeling. The consideration of tensile modulus using bimodular elasticity theory was found to significantly alter the stress and strain distributions in asphalt pavements(Katicha *et al.* 2010, Pan *et al.* 2021). However, since AC is a viscoelastic material, the response of the mixture is significantly affected by temperature and loading time. Thus, the bimodular elasticity theory, which assumes the material is elastic, may not be appropriate for viscoelastic AC mixtures. Levenberg (2015) developed a 1D viscoelastic TC model, in which the viscoelastic strain was used as an indicator to determine whether the state is in compression or tension. This model accurately predicted the responses of asphalt specimens under uniaxial load sequences. However, the author noted the need for extending the 1D model to a 3D model to accurately account for the complex stress-strain states in 3D scenarios.

The objective of this study is to develop a constitutive model to capture the TC asymmetry of AC and quantify its effect on pavement performance. To this end, a new constitutive model, called the "dual viscoelastic model", was developed and applied to the pavement modeling. An overview of the research plan is presented in Figure 2. Initially, the dual viscoelastic model was formulated, incorporating the Williams-Landel-Ferry (WLF) equation to account for the temperature dependence of AC. Additionally, a corresponding numerical algorithm for this model was developed and implemented as a user material (UMAT) subroutine in the ABAQUS software. Furthermore, a pavement structure model was developed for numerical modeling. Through numerical modeling, the pavement responses under moving tire load, such as deformation and strains, can be predicted accounting for the TC asymmetry of AC.

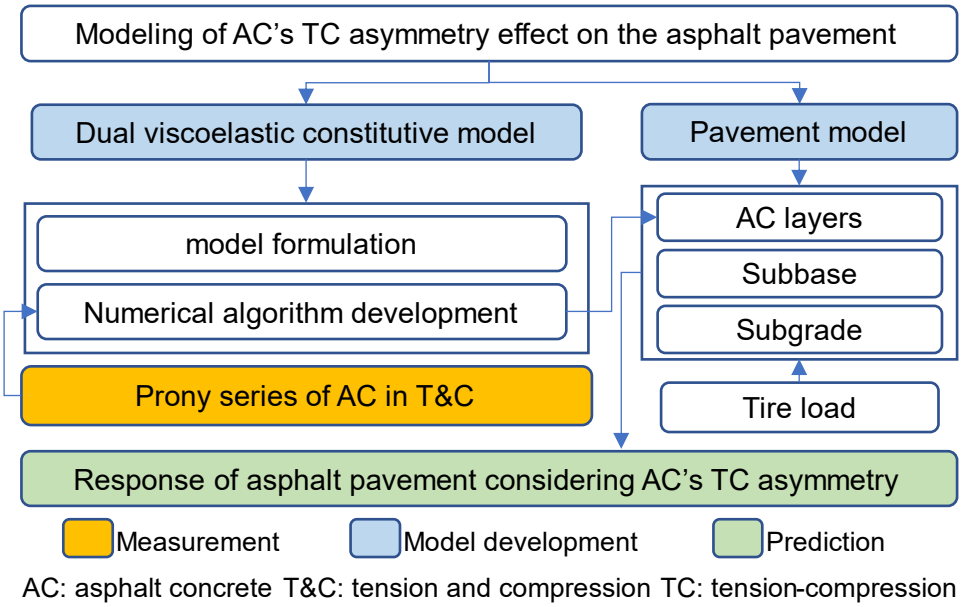

Figure 2 Overview of this study

2. Dual Viscoelastic Model Formulation

For the one-dimensional scenario, the isotropic viscoelastic constitutive model can be expressed as follows:

$$\sigma(\tau)=\int_0^{\tau}E(\tau-\tau')\dot{\varepsilon}d\tau' \tag{1}$$

where $\sigma(\tau)$ is the stress; τ is the reduced time; τ' is the time integration variable; and $E(\tau)$ is the relaxation elastic modulus, which is a function of the reduced time τ. $\dot{\varepsilon}$ is the derivative of stain with respect to τ'. In three dimensions, the stress (σ_{ij}) and strain tensors (ε_{ij}) are often separated into two components: deviatoric and volumetric components. Thus, the 3D viscoelastic constitutive equation can be written as:

$$\sigma_{ij}(\tau)=\int_0^{\tau}2G(\tau-\tau')\dot{e}_{ij}d\tau'+\delta_{ij}\int_0^{\tau}K(\tau-\tau')\dot{\varepsilon}_v d\tau' \tag{2}$$

where $\dot{e}_{ij}$ and $\dot{\varepsilon}_v$ are the derivatives of deviatoric and volumetric strains with respect to τ', respectively; δ_{ij} is the second-order unit tensor; and G and K are the shear and bulk relaxation moduli, which are functions of reduced time τ. Generally, Prony series representation, also called the generalized Maxwell model, is used to describe the relaxation elastic modulus. It can be expressed as (Tschoegl 1989, Lakes 1998, Cho 2016):

$$E(\tau)=E_{\infty}+\sum_{k=1}^{N}E_k e^{-\tau/\tau_k}=E_0\left(1-\sum_{k=1}^{N}g_k\left(1-e^{-\tau/\tau_k}\right)\right) \quad (3)$$

where E_{∞} and $E_0=E_{\infty}+\sum_{k=1}^{N}E_k$ are the long-term and instantaneous elastic moduli; E_k, τ_k, and $g_k=E_k/E_0$ are the elastic modulus, relaxation time and relative modulus of the k th Maxwell element; and N is the number of Maxwell elements. In this study, the Poisson's ratio is assumed unchanged, and the same relaxation times for the Maxwell elements (τ_k) are adopted for the elastic, shear, and bulk relaxation moduli. Thus, the shear and bulk relaxation moduli can be expressed using the same g_k, τ_k, and N as follows:

$$G(\tau)=G_{\infty}+\sum_{k=1}^{N}G_k e^{-\tau/\tau_k}=G_0\left(1-\sum_{k=1}^{N}g_k\left(1-e^{-\tau/\tau_k}\right)\right) \quad (4)$$

$$K(\tau)=K_{\infty}+\sum_{k=1}^{N}K_k e^{-\tau/\tau_k}=K_0\left(1-\sum_{k=1}^{N}g_k\left(1-e^{-\tau/\tau_k}\right)\right) \quad (5)$$

where G_0 and K_0 represent the instantaneous shear and instantaneous bulk moduli. However, the isotropic viscoelastic model is direction-independent, with isotropic relaxation functions for material in T&C. To make this model applicable for the direction-dependent AC, the relaxation moduli are correlated to the volumetric strain (ε_v). If $\varepsilon_v<0$, the compressive relaxation moduli ($E^{-}(\tau)$, $G^{-}(\tau)$ and $K^{-}(\tau)$) are adopted. Otherwise, the relaxation moduli in tension ($E^{+}(\tau)$, $G^{+}(\tau)$ and $K^{+}(\tau)$) are used. The reason why the volumetric strain is selected as the TC indicator is based on the microstructural contact characteristics of AC in T&C. As aforementioned, the TC asymmetry is induced by the contact and separation between aggregates in T&C, respectively. Thus, the element in contraction due to compression or expansion due to tension can be manifested by the sign of volumetric strain. Accordingly, the relaxation moduli for asymmetric AC should be capable of switching between tensile and compressive relaxation moduli according to the sign of ε_v. In this manner, the direction-independent relaxation functions of Eqs. (3) to (5) can be converted to the following direction-dependent relaxation functions:

$$E(\tau)=H(-\varepsilon_v)E_0^{-}\left(1-\sum_{k=1}^{N^{-}}g_k^{-}\left(1-e^{-\tau/\tau_k^{-}}\right)\right)+H(\varepsilon_v)E_0^{+}\left(1-\sum_{k=1}^{N^{+}}g_k^{+}\left(1-e^{-\tau/\tau_k^{+}}\right)\right) \quad (6)$$

$$G(\tau)=H(-\varepsilon_v)G_0^{-}\left(1-\sum_{k=1}^{N^{-}}g_k^{-}\left(1-e^{-\tau/\tau_k^{-}}\right)\right)+H(\varepsilon_v)G_0^{+}\left(1-\sum_{k=1}^{N^{+}}g_k^{+}\left(1-e^{-\tau/\tau_k^{+}}\right)\right) \quad (7)$$

$$K(\tau)=H(-\varepsilon_v)K_0^-\left(1-\sum_{k=1}^{N^-}g_k^-\left(1-e^{-\tau/\tau_k^-}\right)\right)+H(\varepsilon_v)K_0^+\left(1-\sum_{k=1}^{N^+}g_k^+\left(1-e^{-\tau/\tau_k^+}\right)\right) \tag{8}$$

where the superscripts $(\cdot)^-$ and $(\cdot)^+$ represent the variables in compression and tension, respectively; and $H(\cdot)$ is the Heaviside step function. Due to the differences in relaxation moduli, the deviatoric and volumetric stains should also be divided into compressive and tensile parts based on the sign of ε_v, as follows:

$$e_{ij}=\int_0^\tau H(-\varepsilon_v)\frac{de_{ij}}{d\tau'}d\tau'+\int_0^\tau H(\varepsilon_v)\frac{de_{ij}}{d\tau'}d\tau'=e_{ij}^-+e_{ij}^+ \tag{9}$$

$$\varepsilon_v=\int_0^\tau H(-\varepsilon_v)\frac{d\varepsilon_v}{d\tau'}d\tau'+\int_0^\tau H(\varepsilon_v)\frac{d\varepsilon_v}{d\tau'}d\tau'=\varepsilon_v^-+\varepsilon_v^+ \tag{10}$$

Based on Eq. (9) and (10), the following differential expressions can be derived:

$$de_{ij}^-=H(-\varepsilon_v)de_{ij} \tag{11}$$

$$de_{ij}^+=H(\varepsilon_v)de_{ij} \tag{12}$$

$$d\varepsilon_v^-=H(-\varepsilon_v)d\varepsilon_v \tag{13}$$

$$d\varepsilon_v^+=H(\varepsilon_v)d\varepsilon_v \tag{14}$$

Based on the tensile and compressive strains, the resultant stress can be separated into the compressive and tensile parts as follows:

$$\sigma_{ij}=\sigma_{ij}^-+\sigma_{ij}^+ \tag{15}$$

where σ_{ij}^- and σ_{ij}^+ denote the stress induced by compression and tension, respectively. By substituting Eqs. (7) and (8) into Eq. (2), the compressive and tensile parts of stress can be written as follows:

$$\begin{aligned}\sigma_{ij}^- &= 2\int_0^\tau H(-\varepsilon_v)G_0^-\left(1-\sum_{k=1}^{N^-}g_k^-\left(1-e^{(\tau'-\tau)/\tau_k^-}\right)\right)\frac{de_{ij}}{d\tau'}d\tau'+\delta_{ij}\int_0^\tau H(-\varepsilon_v)K_0^-\left(1-\sum_{k=1}^{N^-}g_k^-\left(1-e^{(\tau'-\tau)/\tau_k^-}\right)\right)\frac{d\varepsilon_v}{d\tau'}d\tau' \\ &= 2\int_0^\tau G_0^-\left(1-\sum_{k=1}^{N^-}g_k^-\left(1-e^{(\tau'-\tau)/\tau_k^-}\right)\right)\frac{de_{ij}H(-\varepsilon_v)}{d\tau'}d\tau'+\delta_{ij}\int_0^\tau K_0^-\left(1-\sum_{k=1}^{N^-}g_k^-\left(1-e^{(\tau'-\tau)/\tau_k^-}\right)\right)\frac{d\varepsilon_v H(-\varepsilon_v)}{d\tau'}d\tau' \\ &= 2\int_0^\tau G_0^-\left(1-\sum_{k=1}^{N^-}g_k^-\left(1-e^{(\tau'-\tau)/\tau_k^-}\right)\right)\frac{de_{ij}^-}{d\tau'}d\tau'+\delta_{ij}\int_0^\tau K_0^-\left(1-\sum_{k=1}^{N^-}g_k^-\left(1-e^{(\tau'-\tau)/\tau_k^-}\right)\right)\frac{d\varepsilon_v^-}{d\tau'}d\tau'\end{aligned} \tag{16}$$

$$\sigma_{ij}^{+}=2\int_0^{\tau}H(\varepsilon_v)G_0^{+}\left(1-\sum_{k=1}^{N^{+}}g_k^{+}\left(1-e^{(\tau'-\tau)/\tau_k^{+}}\right)\right)\frac{de_{ij}}{d\tau'}d\tau'+\delta_{ij}\int_0^{\tau}H(\varepsilon_v)K_0^{+}\left(1-\sum_{k=1}^{N^{+}}g_k^{+}\left(1-e^{(\tau'-\tau)/\tau_k^{+}}\right)\right)\frac{d\varepsilon_v}{d\tau'}d\tau'$$

$$=2\int_0^{\tau}G_0^{+}\left(1-\sum_{k=1}^{N^{+}}g_k^{+}\left(1-e^{(\tau'-\tau)/\tau_k^{+}}\right)\right)\frac{de_{ij}H(\varepsilon_v)}{d\tau'}d\tau'+\delta_{ij}\int_0^{\tau}K_0^{+}\left(1-\sum_{k=1}^{N^{+}}g_k^{+}\left(1-e^{(\tau'-\tau)/\tau_k^{+}}\right)\right)\frac{d\varepsilon_vH(\varepsilon_v)}{d\tau'}d\tau' \quad (17)$$

$$=2\int_0^{\tau}G_0^{+}\left(1-\sum_{k=1}^{N^{+}}g_k^{+}\left(1-e^{(\tau'-\tau)/\tau_k^{+}}\right)\right)\frac{de_{ij}^{+}}{d\tau'}d\tau'+\delta_{ij}\int_0^{\tau}K_0^{+}\left(1-\sum_{k=1}^{N^{+}}g_k^{+}\left(1-e^{(\tau'-\tau)/\tau_k^{+}}\right)\right)\frac{d\varepsilon_v^{+}}{d\tau'}d\tau'$$

Eqs. (15) to (17) correlate the stress to the tensile and compressive strains, which makes the developed constitutive model direction dependent. Furthermore, to take the pavement's temperature into consideration, the WLF equation was incorporated into the developed model. This equation is based on the time-temperature superposition principle, which relates the reduced time (τ) at the reference temperature (T_r) to the actual time (t) at the actual temperature (T). The WLF equation is shown below:

$$\log(a_T)=-\frac{C_1\left(T-T_r\right)}{C_2+\left(T-T_r\right)} \quad (18)$$

where a_T is the shift factor; and C_1 and C_2 are the fitted parameters. The shift factor relates the reduced time to the actual time, t, as follows:

$$\tau=\int_0^t\frac{dt'}{a_T} \quad (19)$$

or

$$\frac{d\tau}{dt}=\frac{1}{a_T} \quad (20)$$

In this manner, the reduced time at the reference temperature was converted to the actual time at the real temperature. Thus, the temperature-dependent dual viscoelastic constitutive model was formulated. In this study, T is a function dependent on pavement depth, but independent of the actual time, t. Thus, the temperature-dependent dual viscoelastic model was formulated.

3. Numerical Algorithm Development

The stress and strain increment format for the developed dual viscoelastic model should be derived

for numerical simulation. As the stress function in compression (Eq. (16)) is analogous to the expression in tension (Eq. (17)), the tension format can also be obtained in the same manner if the increment format for compression is derived. In Eq. (16), the first integral term is the deviatoric part stress, which can be written as:

$$\begin{aligned} s_{ij}^{-} &= 2\int_0^{\tau} G_0^{-}\left(1-\sum_{k=1}^{N^{-}} g_k^{-}\left(1-e^{(\tau'-\tau)/\tau_k^{-}}\right)\right)\frac{de_{ij}^{-}}{d\tau'}d\tau' \\ &= 2G_0^{-}\left(\int_0^{\tau}\frac{de_{ij}^{-}}{d\tau'}d\tau' - \int_0^{\tau}\sum_{k=1}^{N^{-}} g_k^{-}\left(1-e^{(\tau'-\tau)/\tau_k^{-}}\right)\frac{de_{ij}^{-}}{d\tau'}d\tau'\right) \\ &= 2G_0^{-}\left(e_{ij}^{-} - \sum_{k=1}^{N^{-}} g_k^{-}\int_0^{\tau}\left(1-e^{(\tau'-\tau)/\tau_k^{-}}\right)\frac{de_{ij}^{-}}{d\tau'}d\tau'\right) \end{aligned} \tag{21}$$

Let $e_{ij}^{k,-} = \int_0^{\tau}\left(1-e^{(\tau'-\tau)/\tau_k^{-}}\right)\frac{de_{ij}^{-}}{d\tau'}d\tau'$. Thus, $e_{ij}^{k,-}$ at the n and $n+1$ steps are

$$e_{ij,n}^{k,-} = \int_0^{\tau_n}\left(1-e^{(\tau'-\tau_n)/\tau_k^{-}}\right)\frac{de_{ij}^{-}}{d\tau'}d\tau' \tag{22}$$

$$e_{ij,n+1}^{k,-} = \int_0^{\tau_{n+1}}\left(1-e^{\frac{\tau'-\tau_{n+1}}{\tau_k^{-}}}\right)\frac{de_{ij}^{-}}{d\tau'}d\tau' = \int_0^{\tau_n}\left(1-e^{(\tau'-\tau_n)/\tau_k^{-}}\right)\frac{de_{ij}^{-}}{d\tau'}d\tau' + \int_{\tau_n}^{\tau_{n+1}}\left(1-e^{(\tau'-\tau_{n+1})/\tau_k^{-}}\right)\frac{de_{ij}^{-}}{d\tau'}d\tau' \tag{23}$$

It can be observed that

$$1-e^{(\tau'-\tau_{n+1})/\tau_k^{-}} = 1-e^{-\Delta\tau_n/\tau_k^{-}} + e^{-\Delta\tau_n/\tau_k^{-}}\left(1-e^{(\tau'-\tau_n)/\tau_k^{-}}\right) \tag{24}$$

where $\Delta\tau_n$ is the time increment at the n step; and $\tau_{n+1} = \tau_n + \Delta\tau_n$. Besides, use the approximation of $\frac{de_{ij}^{-}}{d\tau'} \approx \frac{\Delta e_{ij,n}^{-}}{\Delta\tau_n}$, Eq. (23) can be rewritten as follows:

$$e_{ij,n+1}^{k,-} = \left(1-e^{-\Delta\tau_n/\tau_k^{-}}\right)\int_0^{\tau_n}\frac{de_{ij}^{-}}{d\tau'}d\tau' + e^{-\Delta\tau_n/\tau_k^{-}}\int_0^{\tau_n}\left(1-e^{(\tau'-\tau_n)/\tau_k^{-}}\right)\frac{de_{ij}^{-}}{d\tau'}d\tau' + \frac{\Delta e_{ij,n}^{-}}{\Delta\tau_n}\int_{\tau_n}^{\tau_{n+1}}\left(1-e^{(\tau'-\tau_{n+1})/\tau_k^{-}}\right)d\tau' \tag{25}$$

where $\Delta e_{ij,n}^{-}$ is the compressive deviatoric strain increment at step n. In this equation, the first term is $\left(1-e^{-\Delta\tau_n/\tau_k^{-}}\right)\int_0^{\tau_n}\frac{de_{ij}^{-}}{d\tau'}d\tau' = \left(1-e^{-\Delta\tau_n/\tau_k^{-}}\right)e_{ij,n}^{-}$. Compared with Eq. (22), it can be found that the second integral represents the viscous strain in the k th term at the n increment, which is $e_{ij,n}^{k,-}$; and the third integral can

be readily evaluated, which is $\left(\Delta\tau_n - \tau_k^-\left(1-e^{-\Delta\tau_n/\tau_k^-}\right)\right)$. Thus, the change in the k th viscous deviatoric strain at increment n is

$$\begin{aligned}\Delta e_{ij,n}^{k,-} &= \left(1-e^{-\Delta\tau_n/\tau_k^-}\right)\frac{\Delta\tau_n}{\tau_k^-}e_{ij,n}^- + \left(e^{-\Delta\tau_n/\tau_k^-}-1\right)e_{ij,n}^{k,-} + \frac{\Delta e_{ij,n}^-}{\Delta t_n}\left(\Delta\tau_n - \tau_k^-\left(1-e^{-\Delta\tau_n/\tau_k^-}\right)\right) \\ &= \frac{\tau_k^-}{\Delta\tau_n}\left(\frac{\Delta\tau_n}{\tau_k^-}+e^{-\Delta\tau_n/\tau_k^-}-1\right)\Delta e_{ij,n}^- + \left(1-e^{-\Delta\tau_n/\tau_k^-}\right)\left(e_{ij,n}^- - e_{ij,n}^{k,-}\right)\end{aligned} \tag{26}$$

If $\frac{\Delta\tau_n}{\tau_k^-}$ approaches zero ($\Delta\tau_n/\tau_k^- < 10^{-7}$), this expression can be approximated by

$$\Delta e_{ij,n}^{k,-} = \frac{\Delta\tau_n}{\tau_k^-}\left(\frac{1}{2}\Delta e_{ij,n}^- + e_{ij,n}^- - e_{ij,n}^{k,-}\right) \tag{27}$$

The deviatoric stress increment can be calculated as follows:

$$\Delta s_{ij,n}^- = 2G_0^-\left(\Delta e_{ij,n}^- - \sum\nolimits_{k=1}^{N^-} g_k^- \Delta e_{ij,n}^{k,-}\right) \tag{28}$$

In Eq. (16), it can be observed that the volumetric part expression is similar to the deviatoric part. Thus, the volumetric part strain and stress have the analogous expressions as follows:

$$\sigma_v^- = K_0^-\left(\varepsilon_v^- - \sum\nolimits_{k=1}^{N^-} g_k^- \int_0^\tau \left(1-e^{(\tau'-\tau)/\tau_k^-}\right)\frac{d\varepsilon_v^-}{d\tau'}d\tau'\right) \tag{29}$$

$$\Delta\varepsilon_{v,n}^{k,-} = \begin{cases} \frac{\tau_k^-}{\Delta\tau_n}\left(\frac{\Delta\tau_n}{\tau_k^-}+e^{-\frac{\Delta\tau_n}{\tau_k^-}}-1\right)\Delta\varepsilon_{v,n}^- + \left(1-e^{-\frac{\Delta\tau_n}{\tau_k^-}}\right)\left(\varepsilon_{v,n}^- - \varepsilon_{v,n}^{k,-}\right) & \text{if } \frac{\Delta\tau_n}{\tau_k^-} \geq 10^{-7} \\ \frac{\Delta\tau_n}{\tau_k^-}\left(\frac{1}{2}\Delta\varepsilon_{v,n}^- + \varepsilon_{v,n}^- - \varepsilon_{v,n}^{k,-}\right) & \text{if } \frac{\Delta\tau_n}{\tau_k^-} < 10^{-7} \end{cases} \tag{30}$$

$$\Delta\sigma_{v,n}^- = K_0^c\left(\Delta\varepsilon_{v,n}^c - \sum\nolimits_{k=1}^{N^c} g_k \Delta\varepsilon_{v,n}^k\right) \tag{31}$$

where σ_v^-, $\Delta\varepsilon_{v,n}^{k,-}$, and $\Delta\sigma_{v,n}^-$ are the volumetric part stress, the k th viscous volumetric strain increment, and the volumetric stress increment at step n.

Analogously, the deviatoric and volumetric stresses for the tension part can also be obtained. Combining the resultant stresses caused by T&C, the stresses at $n+1$ step can be derived as follows:

$$s_{ij,n+1} = s_{ij,n} + \Delta s_{ij,n}^- + \Delta s_{ij,n}^+ \tag{32}$$

$$\sigma_{v,n+1} = \sigma_{v,n} + \Delta\sigma_{v,n}^- + \Delta\sigma_{v,n}^+ \tag{33}$$

The tangent shear modulus (G^T) and bulk modulus (K^T) are readily derived by differentiating the deviatoric stress increment ($\Delta s_{ij,n}^- + \Delta s_{ij,n}^+$) with respect to the deviatoric strain ($\Delta e_{ij,n}^- + \Delta e_{ij,n}^+$) and volumetric stress increment ($\Delta \sigma_{v,n}^- + \Delta \sigma_{v,n}^+$) with respect to the volumetric strain ($\Delta \varepsilon_{v,n}$), respectively, as follows:

$$G^T = H\left(-\varepsilon_v\right) G^{T,-} + H\left(\varepsilon_v\right) G^{T,+} \tag{34}$$

$$K^T = H\left(-\varepsilon_v\right) K^{T,-} + H\left(\varepsilon_v\right) K^{T,+} \tag{35}$$

where

$$G^{T,-} = \begin{cases} G_0^- \left[1 - \sum_{k=1}^{N^-} g_k^- \dfrac{\tau_k^-}{\Delta \tau_n} \left(\dfrac{\Delta \tau_n}{\tau_k^-} + e^{\Delta \tau_n / \tau_k^-} - 1 \right) \right] & \text{if } \dfrac{\Delta \tau_n}{\tau_k^-} \geq 10^{-7} \\ G_0^- \left(1 - \sum_{k=1}^{N^-} \dfrac{1}{2} g_k^- \dfrac{\Delta \tau_n}{\tau_k^-} \right) & \text{if } \dfrac{\Delta \tau_n}{\tau_k^-} < 10^{-7} \end{cases}$$

$$G^{T,+} = \begin{cases} G_0^+ \left[1 - \sum_{k=1}^{N^+} g_k^+ \dfrac{\tau_k^+}{\Delta \tau_n} \left(\dfrac{\Delta \tau_n}{\tau_k^-} + e^{\Delta \tau_n / \tau_k^+} - 1 \right) \right] & \text{if } \dfrac{\Delta \tau_n}{\tau_k^+} \geq 10^{-7} \\ G_0^+ \left(1 - \sum_{k=1}^{N^+} \dfrac{1}{2} g_k^+ \dfrac{\Delta \tau_n}{\tau_k^+} \right) & \text{if } \dfrac{\Delta \tau_n}{\tau_k^+} < 10^{-7} \end{cases}$$

$$K^{T,-} = \begin{cases} K_0^- \left[1 - \sum_{k=1}^{N^-} g_k^- \dfrac{\tau_k^-}{\Delta \tau_n} \left(\dfrac{\Delta \tau_n}{\tau_k^-} + e^{\Delta \tau_n / \tau_k^-} - 1 \right) \right] & \text{if } \dfrac{\Delta \tau_n}{\tau_k^-} \geq 10^{-7} \\ K_0^- \left(1 - \sum_{k=1}^{N^-} \dfrac{1}{2} g_k^- \dfrac{\Delta \tau_n}{\tau_k^-} \right) & \text{if } \dfrac{\Delta \tau_n}{\tau_k^-} < 10^{-7} \end{cases}$$

$$K^{T,+} = \begin{cases} K_0^+ \left[1 - \sum_{k=1}^{N^+} g_k^+ \dfrac{\tau_k^+}{\Delta \tau_n} \left(\dfrac{\Delta \tau_n}{\tau_k^+} + e^{\Delta \tau_n / \tau_k^+} - 1 \right) \right] & \text{if } \dfrac{\Delta \tau_n}{\tau_k^+} \geq 10^{-7} \\ K_0^+ \left(1 - \sum_{k=1}^{N^+} \dfrac{1}{2} g_k^+ \dfrac{\Delta \tau_n}{\tau_k^+} \right) & \text{if } \dfrac{\Delta \tau_n}{\tau_k^+} < 10^{-7} \end{cases}$$

Thus, the corresponding Jacobian matrix can be expressed as follows:

$$J=\begin{bmatrix} K^T+\frac{4}{3}G^T & K^T-\frac{2}{3}G^T & K^T-\frac{2}{3}G^T & & & \\ K^T-\frac{2}{3}G^T & K^T+\frac{4}{3}G^T & K^T-\frac{2}{3}G^T & & \hat{0} & \\ K^T-\frac{2}{3}G^T & K^T-\frac{2}{3}G^T & K^T+\frac{4}{3}G^T & & & \\ & & & G^T & 0 & 0 \\ & \hat{0} & & 0 & G^T & 0 \\ & & & 0 & 0 & G^T \end{bmatrix} \tag{36}$$

Besides, it should be pointed out that the numerical simulation is difficult to converge because the discontinuity of the Heaviside function at ε_v equal to zero, which significantly increases the iterations and computational time. Therefore, a sigmoidal function as below was used to replace the Heaviside function:

$$S(\varepsilon_v)=\frac{1}{1+e^{-\alpha\varepsilon_v}} \tag{37}$$

where α is an amplification factor. This function, ranging from 0 to 1, is continuous at any ε_v value. A bigger α value makes the function closer to the Heaviside function. In this study, an α value of 10^4 was used, which can ensure numerical accuracy and also significantly improve numerical simulation convergence. Figure 3 presents the developed algorithm for the proposed dual viscoelastic model. This algorithm was coded as a UMAT subroutine for numerical modeling.

1: Pass $\Delta\varepsilon_{ij,n}$ and Δt_n into UMAT

2: Read the stress $\sigma_{ij,n}$ and the state variables ($\varepsilon^-_{ij,n}, e^{k,-}_{ij,n}, \varepsilon^-_{v,n}, \varepsilon^+_n, e^{k,+}_{ij,n}, \varepsilon^+_{v,n}$) from the last step, i.e., n th step

3: Calculate the volumetric strain $\varepsilon_{v,n+1} = \varepsilon_{v,n} + \Delta\varepsilon_{v,n}$

4: $\Delta\varepsilon^-_{ij,n} = S\left(-\varepsilon_v\right)\Delta\varepsilon_{ij,n}; \Delta\varepsilon^+_n = S\left(\varepsilon_v\right)\Delta\varepsilon_{ij,n}$

5: Calculate $\Delta e^{k,-}_{ij,n}, \Delta\varepsilon^{k,-}_{v,n}, \Delta e^-_{ij,n}, \Delta\varepsilon^-_{v,n}$

6: **If** $\dfrac{\Delta\tau_n}{\tau^-_k} < 10^{-7}$ **then**

7: $$\Delta e^{k,-}_{ij,n} = \frac{\Delta\tau_n}{\tau^-_k}\left(\frac{1}{2}\Delta e^-_{ij,n} + e^-_{ij,n} - e^{k,-}_{ij,n}\right); \Delta\varepsilon^{k,-}_{v,n} = \frac{\Delta\tau_n}{\tau^-_k}\left(\frac{1}{2}\Delta\varepsilon^-_{v,n} + \varepsilon^-_{v,n} - \varepsilon^{k,-}_{v,n}\right)$$

8: Else

9: $$\Delta e^{k,-}_{ij,n} = \frac{\tau^-_k}{\Delta\tau_n}\left(\frac{\Delta\tau_n}{\tau^-_k} + e^{-\frac{\Delta t_n}{\tau^-_k}} - 1\right)\Delta e^-_{ij,n} + \left(1 - e^{-\frac{\Delta\tau_n}{\tau^-_k}}\right)\left(e^-_{ij,n} - e^{k,-}_{ij,n}\right)$$

10: $$\Delta\varepsilon^{k,-}_{v,n} = \frac{\tau^-_k}{\Delta\tau_n}\left(\frac{\Delta\tau_n}{\tau^-_k} + e^{-\frac{\Delta\tau_n}{\tau^-_k}} - 1\right)\Delta\varepsilon^-_{v,n} + \left(1 - e^{-\frac{\Delta\tau_n}{\tau^-_k}}\right)\left(\varepsilon^-_{v,n} - \varepsilon^{k,-}_{v,n}\right)$$

11: End if

12: Calculate $\Delta e^{k,+}_{ij,n}, \Delta\varepsilon^{k,+}_{v,n}, \Delta e^+_{ij,n}, \Delta\varepsilon^+_{v,n}$

13: **If** $\dfrac{\Delta\tau_n}{\tau^+_k} < 10^{-7}$ **then**

14: $$\Delta e^{k,+}_{ij,n} = \frac{\Delta\tau_n}{\tau^+_k}\left(\frac{1}{2}\Delta e^+_{ij,n} + e^+_{ij,n} - e^{k,+}_{ij,n}\right); \Delta\varepsilon^{k,+}_{v,n} = \frac{\Delta\tau_n}{\tau^+_k}\left(\frac{1}{2}\Delta\varepsilon^+_{v,n} + \varepsilon^+_{v,n} - \varepsilon^{k,+}_{v,n}\right)$$

15: Else

16: $$\Delta e^{k,+}_{ij,n} = \frac{\tau^+_k}{\Delta t_n}\left(\frac{\Delta\tau_n}{\tau^+_k} + e^{-\frac{\Delta\tau_n}{\tau^+_k}} - 1\right)\Delta e^+_{ij,n} + \left(1 - e^{-\frac{\Delta\tau_n}{\tau^+_k}}\right)\left(e^+_{ij,n} - e^{k,+}_{ij,n}\right).$$

17: $$\Delta\varepsilon^{k,+}_{v,n} = \frac{\tau^+_k}{\Delta\tau_n}\left(\frac{\Delta\tau_n}{\tau^+_k} + e^{-\frac{\Delta\tau_n}{\tau^+_k}} - 1\right)\Delta\varepsilon^+_{v,n} + \left(1 - e^{-\frac{\Delta\tau_n}{\tau^+_k}}\right)\left(\varepsilon^+_{v,n} - \varepsilon^{k,+}_{v,n}\right)$$

18: End if

19: Calculate $\Delta s^-_{ij}, \Delta\sigma^-_v, \Delta s^+_{ij}, \Delta\sigma^+_v$

20: $$\Delta s^-_{ij,n} = 2G^-_0\left(\Delta e^-_{ij,n} - \sum\nolimits_{k=1}^{N^-} g^-_k \Delta e^{k,-}_{ij,n}\right); \Delta\sigma^-_{v,n} = K^-_0\left(\Delta\varepsilon^-_{v,n} - \sum\nolimits_{k=1}^{N^-} g^-_k \Delta\varepsilon^{k,-}_{v,n}\right)$$

21: $$\Delta s^+_{ij,n} = 2G^+_0\left(\Delta e^+_{ij,n} - \sum\nolimits_{k=1}^{N^+} g^+_k \Delta e^{k,+}_{ij,n}\right); \Delta\sigma^+_{v,n} = K^+_0\left(\Delta\varepsilon^+_{v,n} - \sum\nolimits_{k=1}^{N^+} g^+_k \Delta\varepsilon^{k,+}_{v,n}\right).$$

22: Calculate $\sigma_{ij,n+1}$

23: $$\sigma_{ij,n+1} = \sigma_{ij,n} + \Delta s^-_{ij,n} + \delta_{ij}\Delta\sigma^-_{v,n} + \Delta s^+_{ij,n} + \delta_{ij}\Delta\sigma^+_{v,n}$$

24: Update state variables ($\varepsilon^-_{ij,n+1}, e^{k,-}_{ij,n+1}, \varepsilon^-_{v,n+1}, \varepsilon^+_{ij,n+1}, e^{k,+}_{ij,n+1}, \varepsilon^+_{v,n+1}$)

25: . $\varepsilon^-_{ij,n+1} = \varepsilon^-_{ij,n} + \Delta\varepsilon^-_{ij,n}; e^{k,-}_{ij,n+1} = e^{k,-}_{ij,n} + \Delta e^{k,-}_{ij,n}; \varepsilon^-_{v,n+1} = \varepsilon^-_{v,n} + \Delta\varepsilon^-_{v,n}$.

26: $\varepsilon^{+}_{ij,n+1} = \varepsilon^{+}_{ij,n} + \Delta\varepsilon^{+}_{ij,n}; e^{k,+}_{ij,n+1} = e^{k,+}_{ij,n} + \Delta e^{k,+}_{ij,n}; \varepsilon^{+}_{v,n+1} = \varepsilon^{+}_{v,n} + \Delta\varepsilon^{+}_{v,n}$

27: Calculate Jacobian matrix (DDSDDE)

Figure 3 Numerical algorithm of the dual viscoelastic constitutive model

4. Model Validation

In this study, a unit eight-node linear brick element (C3D8) model was utilized to validate the developed user material (UMAT) subroutine for the proposed dual viscoelastic constitutive model (Figure 4(a)). This evaluation on the unit element model can make the evaluate on the develop UMAT code easier and efficiency. To evaluate the accuracy, robustness, and versatility of the model, three material models were considered: ABAQUS_C, UMAT_CC, and UMAT_TC. ABAQUS_C and UMAT_CC represent the models that only applied compressive viscoelastic properties through the ABAQUS built-in Prony series and the developed UMAT subroutine, respectively. The UMAT_TC model was assigned both tensile and compressive parameters. As discussed in Section 2, the developed dual viscoelastic constitutive model can degenerate into the isotropic viscoelastic model when the same Prony series parameters are used for the model in T&C. Therefore, both ABAQUS_C and UMAT_CC should provide identical predictions. In the simulation, the bottom of the unit element model was fixed, and a 1 Hz sinusoidal load with an amplitude of 1 N was applied to the top surface of the model. Figure 4(b), (c), and (d) present the vertical deformation at 10 s for the three models. The plots from the ABAQUS_C and UMAT_CC models show identical vertical displacement distributions, which essentially validates the developed UMAT code. When both tensile and compressive properties were applied, the UMAT_TC model offered lower compressive displacements (Figure 4(d)). Additionally, the predicted strain curves obtained from different simulations are presented in Figure 5. Identical resultant strain curves are evident from ABAQUS_C and UMAT_CC models. Furthermore, due to the lower tensile than compressive moduli, the UMAT_TC model offered an asymmetric resultant strain curve (in purple) by showing much higher tensile strains than compression. These results verified the accuracy of the developed dual viscoelastic constitutive model in capturing AC's

TC asymmetry. Overall, this exercise demonstrates that the developed UMAT subroutine is also applicable to complicated dynamic simulations, and the dual viscoelastic constitutive model can accurately capture AC's TC asymmetry.

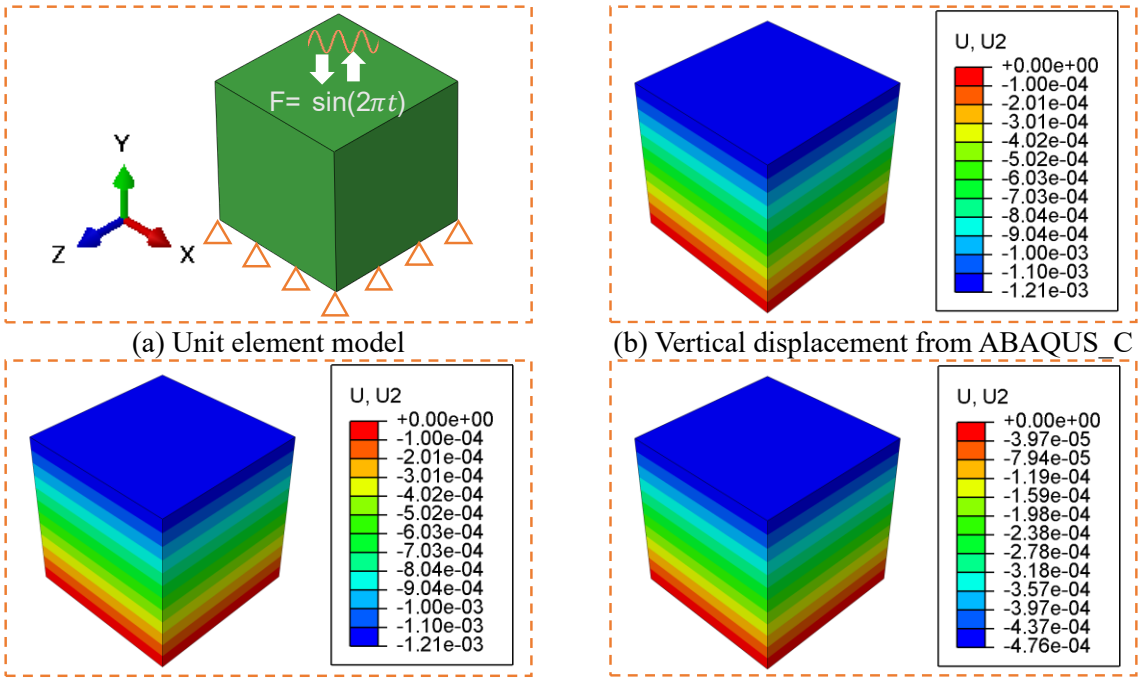

(a) Unit element model (b) Vertical displacement from ABAQUS_C

(c) Vertical displacement from UMAT_CC (d) Vertical displacement from UMAT_TC

Figure 4 The unit element model and the vertical displacement of models at 10s

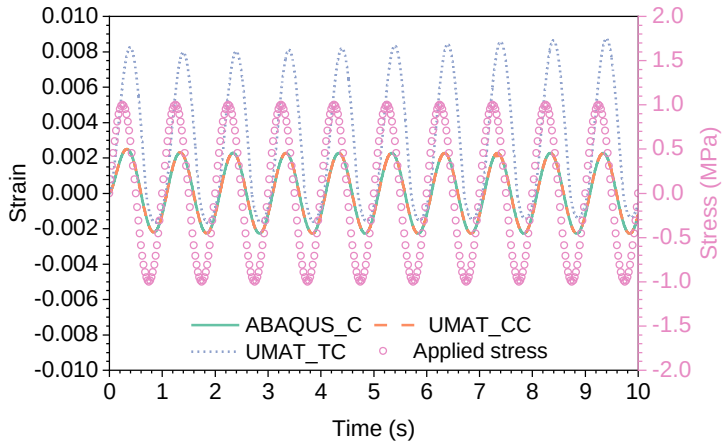

Figure 5 Inputting stress and the resultant strain curves

5. Asphalt Pavement Model

To investigate the impact of AC's TC asymmetry on asphalt pavement response, a pavement structure model was developed (Figure 6(a)). The model dimensions were 6 m in length, 3 m in width and depth, and it consisted of five layers, including the wearing course (WC), base course (BC), road base (RB), subbase,

and subgrade. These layers were constructed based on the typical asphalt pavement structure in Hong Kong, with thicknesses of 40 mm, 65 mm, 175 mm, 225 mm, and 2495 mm, respectively, from top to bottom. As shown in Figure 6(b), the mesh of the loading path zone along the centerline was densified, and transition elements were utilized to gradually increase the element size from fine to coarse. This approach allowed for a significant reduction in the number of elements, while ensuring modeling accuracy. Consequently, the final mesh size around the loading path is 40 mm in both the X and Y directions. In the depth dimension, the WC, BC, and RB layers are meshed with 2, 3, and 9 element layers, resulting in mesh sizes of approximately 20 mm in the Z direction. In the simulation, the bottom face of the model was fixed, and all lateral faces were constrained in their normal directions. Besides, the different layers were assumed to be well bonded. Therefore, the neighboring layers share their nodes at the interface. The DLOAD subroutine was used to apply the dual-tire load on the top surface (Figure 6(c)) [40]. Two different vehicular speeds, 20 and 80 km/h, were adopted to consider the low and high speeds, respectively. The viscoelastic properties of a gap-graded mixture, SMA10, were incorporated into the top AC layer (WC layer), while the dense-graded AC20 was assigned to the BC and RB layers. Figure 7 presents the master curves of both AC mixtures in T&C (Tan, Leng, *et al.* 2023). It is evident that AC demonstrates a notably lower modulus and a higher phase angle at low frequencies under tension compared to compression. This elastic behavior can be attributed to the presence of aggregate inclusions and physiochemical stiffening. This observation suggests that AC behaves more viscously but less elastically under tension than compression. The subbase and subgrade layers were graded aggregate and soil, respectively, and both layers were regarded as elastic materials. The material properties for all pavement layers are summarized in Table 1. Besides, it should be pointed out that while varying the thickness of AC layers may impact stress/strain levels in the pavement, the influence of AC's TC asymmetry on pavement behavior remains consistent.

In the context of realistic scenarios and pavement design practices, the pavement modeling examines

two scenarios for AC layers: one incorporating AC's TC properties and the other considering only AC's compressive properties (CC). The scenario solely considering AC's tensile properties (TT) is omitted because it does not accurately reflect real pavement conditions and could result in unrealistically high pavement deformation. Two material models: UMAT_TC and UMAT_CC, were utilized to apply the viscoelastic properties of AC mixtures to AC layers. Following the definition in the previous section, UMAT_TC represents the model accounting for both the properties in T&C, while UMAT_CC refers to the model with compressive viscoelastic properties only. Given that temperature is a critical factor affecting the mechanical performance of AC, the real temperature field of pavements should be incorporated into the modeling process. Figure 8(a) shows the measured pavement temperature at different depths on a summer day in the Guangzhou region of China, where the pavement temperature can reach approximately 70°C due to the hot weather, and this temperature varies significantly with depth. To account for the temperature effect in simulations, the pavement temperature fields at 6:00 and 14:00 were selected as the low and high service temperatures, respectively, and the exponential functions were used to capture the relationships of temperature with depth, as illustrated in Figure 8(b). Consequently, eight scenarios were simulated by considering the two material models (UMAT_TC and UMAT_CC) for AC layers, two different vehicular speeds (20 and 80 km/h), and two temperature fields (at 6:00 and 14:00).

Table 1 Material properties for pavement model

Materials	Poisson's ratio	Viscoelasticity/Elasticity
WC layer (SMA10)	0.35	Prony Series (in T&C)*
BC and RB layers (AC20)	0.35	Prony Series (in T&C)*
Subbase	0.3	172.4 MPa
Subgrade	0.35	103.4 MPa

* Prony series parameters can be obtained by converting the master curves (Figure 7) to the Prony series format.

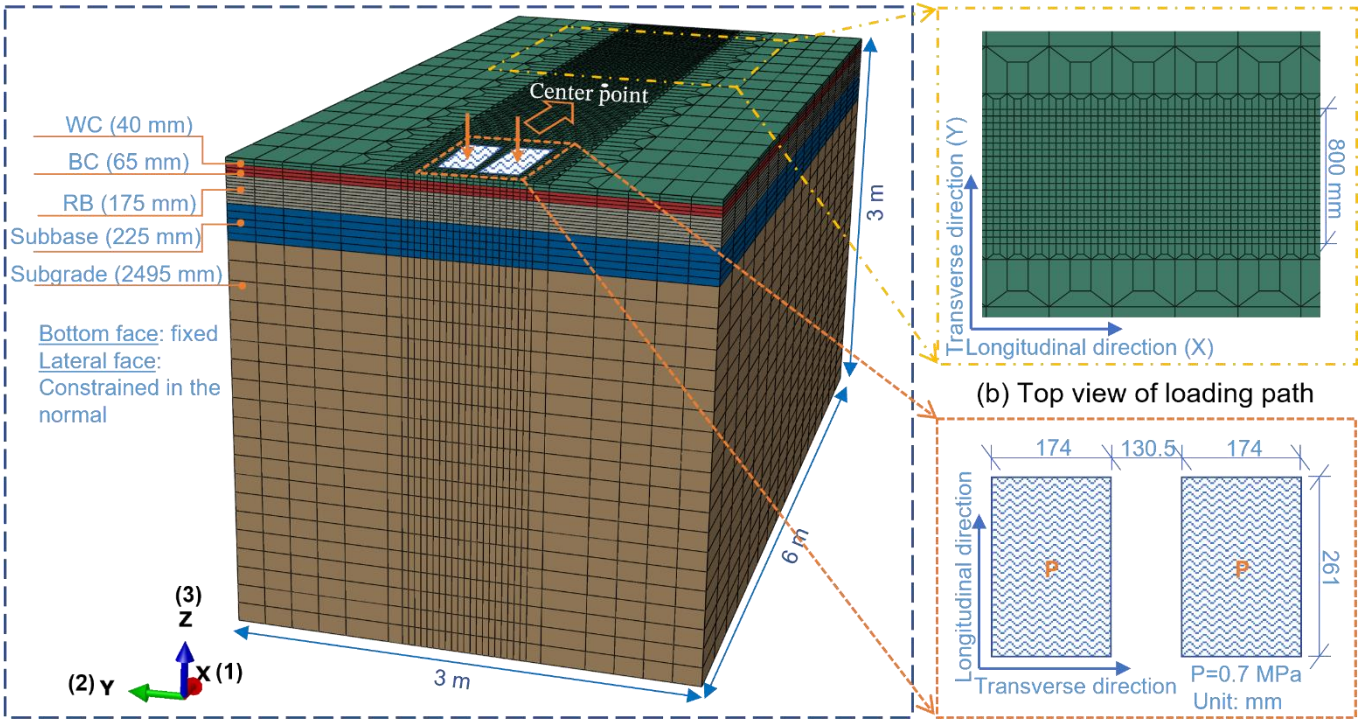

Figure 6 Pavement model setup

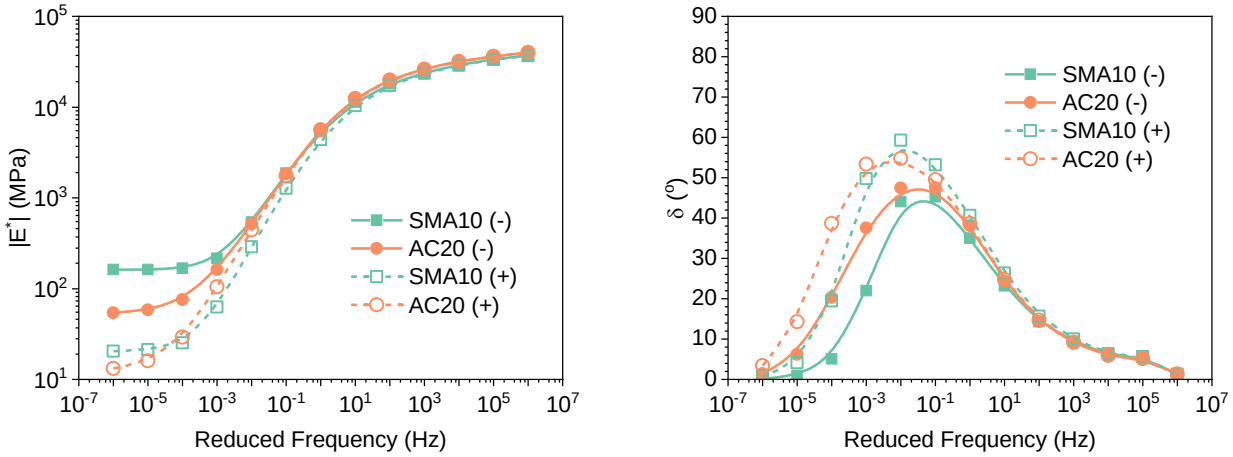

(a) Dynamic modulus (b) Phase angle

Figure 7 Master curves of SMA10 and AC20 in T&C

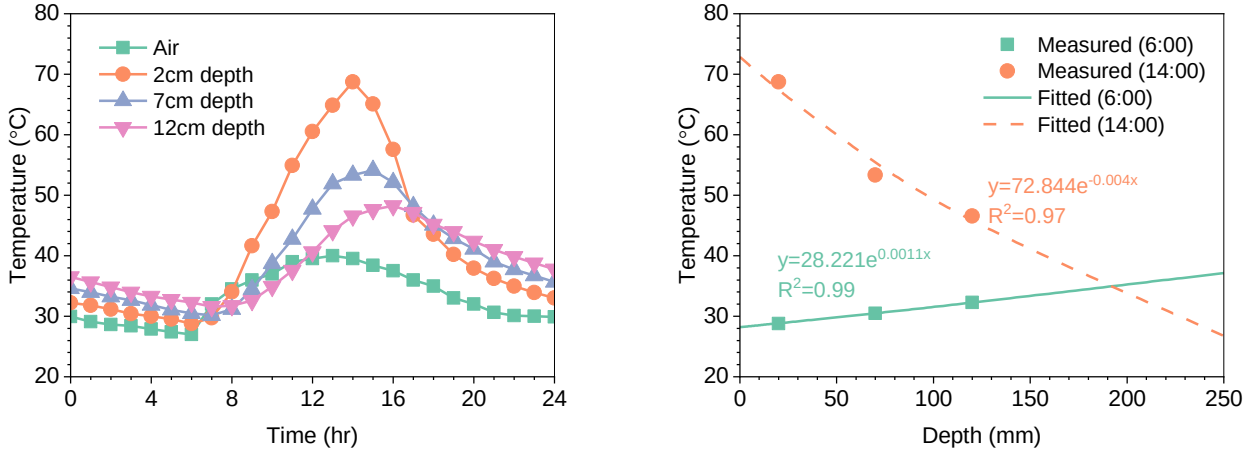

(a) Measured temperatures at different depths (b) Fitted temperature curves at 6:00 and 14:00

Figure 8 Pavement temperatures in summer

6. Results and Discussion

This section presents the analysis of the responses of asphalt pavement under the wheel load. Given that AC exhibits more significant TC asymmetry at high temperatures, the pavement responses at the high temperature profile corresponding to 14:00, as shown in Figure 8(b), were evaluated first. Due to the lower tensile modulus of the UMAT_TC model relative to the conventional UMAT_CC model, it was expected that the UMAT_TC model would result in higher tensile strains and deformations under the tire load. Hence, the vertical deformation (U3) and strains (E11, E22, E33, and E13) were evaluated. Finally, Asphalt pavements at the temperature field at 6:00 were examined to estimate the effects of temperature on pavement responses.

6.1. Vertical deformation (U3) and vertical strain (E33)

Figure 9 presents the vertical deformation (U3) curves on the surface of the middle transverse cross-section of the pavement structure. The curves exhibit two typical troughs within the zones beneath the two tires. As expected, the UMAT_TC model, which has a lower tensile modulus, leads to higher vertical deformations. In particular, the UMAT_TC model increases the highest vertical deformation under the dual-tire load by approximately 6% compared to the UMAT_CC model. Since the current pavement design method exclusively considers compressive properties, such an increase in vertical deformation may indicate an elevated susceptibility to rutting and a potential significant reduction in pavement service life. Furthermore, the results show that vehicular speed is a critical determinant affecting the vertical deformation of the pavement due to the viscoelastic characteristics of AC. At the low vehicular speed (20 km/h), both models produce noticeably higher vertical deformation than at the high vehicular speed (80 km/h).

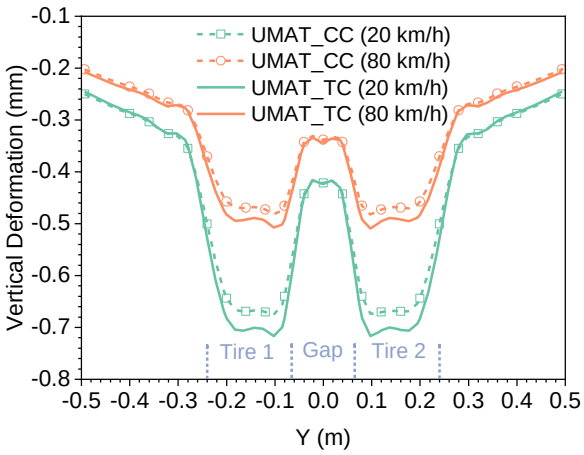

Figure 9 Vertical deformation (U3) at 14:00

To analyze the variations of vertical strain (LE33) within the pavement, the vertical strains along the vertical centerline passing through the center point of pavement surface, as illustrated in Figure 6(a), were evaluated. Figure 10 displays the results for the top 1.0 m depth for simplicity. The analysis reveals that the WC and BC layers experience very high tensile strain. This high value is because the pavement's center is located between the two tires, and the two outside tire loads induce tension in the center zone. Regardless of vehicular speed, the pavement reaches the maximum vertical tensile strain at the interface between WC and BC. This phenomenon can be attributed to the higher strains in the top layers (WC and BC) of pavements induced by the tire load, as well as the strain concentration resulting from the differing material properties of the WC and BC layers at their interface. Compared to the UMAT_CC model, the UMAT_TC model, which considers TC asymmetry, further increases the maximum vertical tensile strain. At a vehicular speed of 20 km/h, the maximum tensile strains for the UMAT_CC and UMAT_TC models are 694 and 843 με, respectively, indicating a 21% increase in the vertical tensile strain for the model considering TC asymmetry.

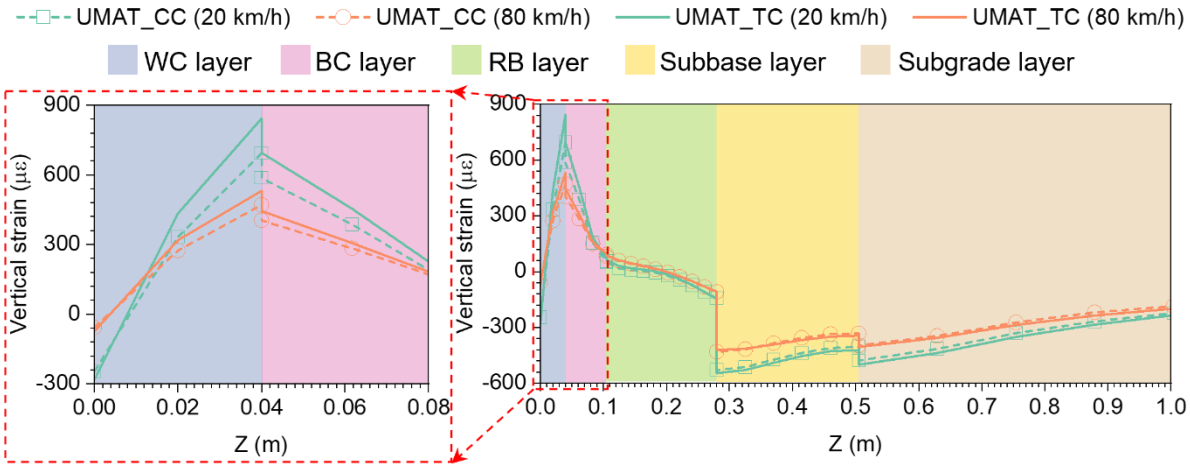

Figure 10 Vertical strain (E33) along the pavement's vertical centerline at 14:00

6.2. Longitudinal strain (E11)

Figure 11 presents the distributions of the strain along the longitudinal direction (E11) in the pavement. Due to the similarity of the strain distributions at the two vehicular speeds, only the strain distributions at 20 km/h are presented. It can be observed that both models exhibit similar strain characteristics, with the front and rear areas of the wheel load showing high positive strains (orange color) indicating tension, and the middle zone (green color) showing compression reflected by negative strain. Furthermore, the strain distributions near the wheels exhibit complex alternations between tensile and compressive strains. High tensile strain is known to lead to fatigue cracking of pavements under repeated traffic loads. Hence, to further analyze the longitudinal strains in the pavement, three transverse cross-sections at the rear (T1), middle (T2), and front (T3) of the tire load, were considered as illustrated in Figure 11(a).

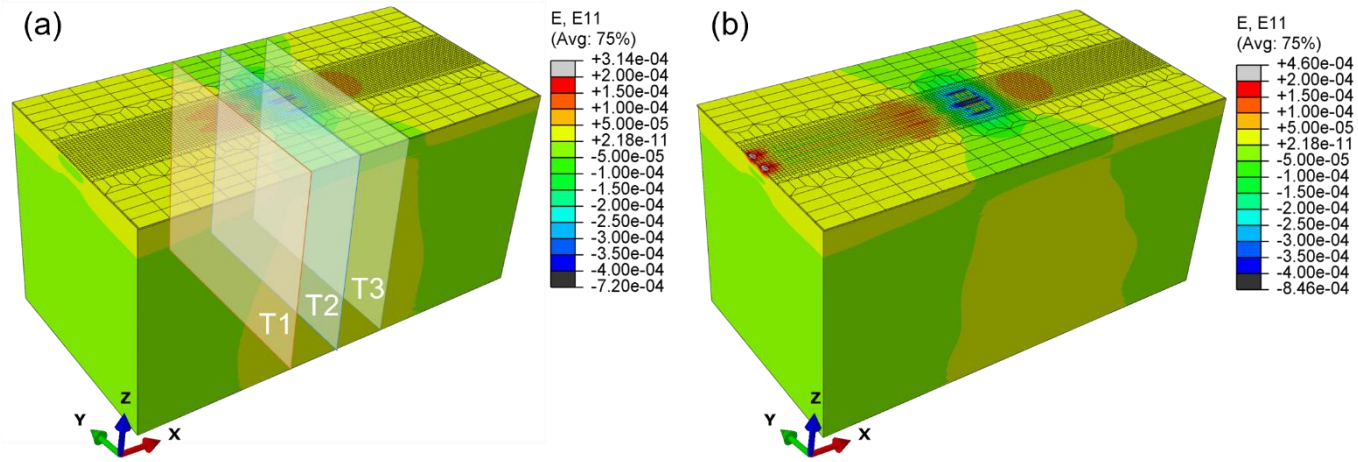

Figure 11 Longitudinal strain (E11) distributions at 20 km/h at high temperature profile (14:00): (a) UMAT_CC model; and (b) UMAT_TC model

The longitudinal strain in three selected transverse cross-sections is presented in Figures 12(a) to (l).

345 The strains from the top surface to the bottom of the three AC layers (WC, BC, and RB) were plotted.
346 Notably, the strain curves in the rear (T1) and middle (T2) cross-sections exhibit changes in troughs and
347 crests, whereas those in the front cross-section (T3) display a parabolic shape with no significant variation.
348 This difference is attributed to the passing of a dual-tire load, with the middle cross-section (T2) being
349 closer to the tire load than the other two sections. Consequently, the tire load has a more substantial impact
350 on the middle section, causing greater changes in strain. Additionally, the figures show that the three AC
351 layers, particularly the top of the WC layer, exhibit high tensile (positive) strains at the transverse sections
352 considered. However, the tensile strains decrease with increasing pavement depths, which contradicts the
353 conventional understanding that the tensile zone is located at the bottom of AC layers. Hence, greater
354 attention should be paid to the tensile strain on the top AC layers in asphalt pavement design. Among the
355 three cross-sections, Figure 12(b) highlights that the middle cross-section beneath the dual-tire load
356 experiences the highest tensile strain (about 400 με). Like the vertical strain (E33), the UMAT_TC model,
357 considering TC asymmetry, further increases the maximum longitudinal strains. Taking the tensile strains
358 in the top of the WC layer as an example, the predicted tensile strains at 20 km/h from the UMAT_TC
359 model are approximately 1.5 times higher than those from the UMAT_CC model at the rear and front
360 sections (Figure 12(a) and (c)). In the middle cross-section (Figure 12(b)), more than a 30% increase in
361 longitudinal tensile strains is still observed for the UMAT_TC model. These results indicate that the TC
362 asymmetry of AC can significantly increase the longitudinal tensile strain on the surface AC layer, making
363 the layer more susceptible to transverse top-down cracking under repeated traffic loads However, the tensile
364 strains in the three cross-sections decrease considerably at higher vehicular speeds of 80 km/h, implying
365 that high vehicular speeds can reduce longitudinal strains and minimize the effect of TC asymmetry on
366 asphalt pavement. It should be noted that there are many other important factors, including climate effects,
367 that can lead to top-down cracking. Nevertheless, it is important to emphasize that AC's TC asymmetry can

lead to an increase in high tensile strain on the pavement surface, which may contribute to top-down cracking. This aspect has not been extensively explored in prior studies.

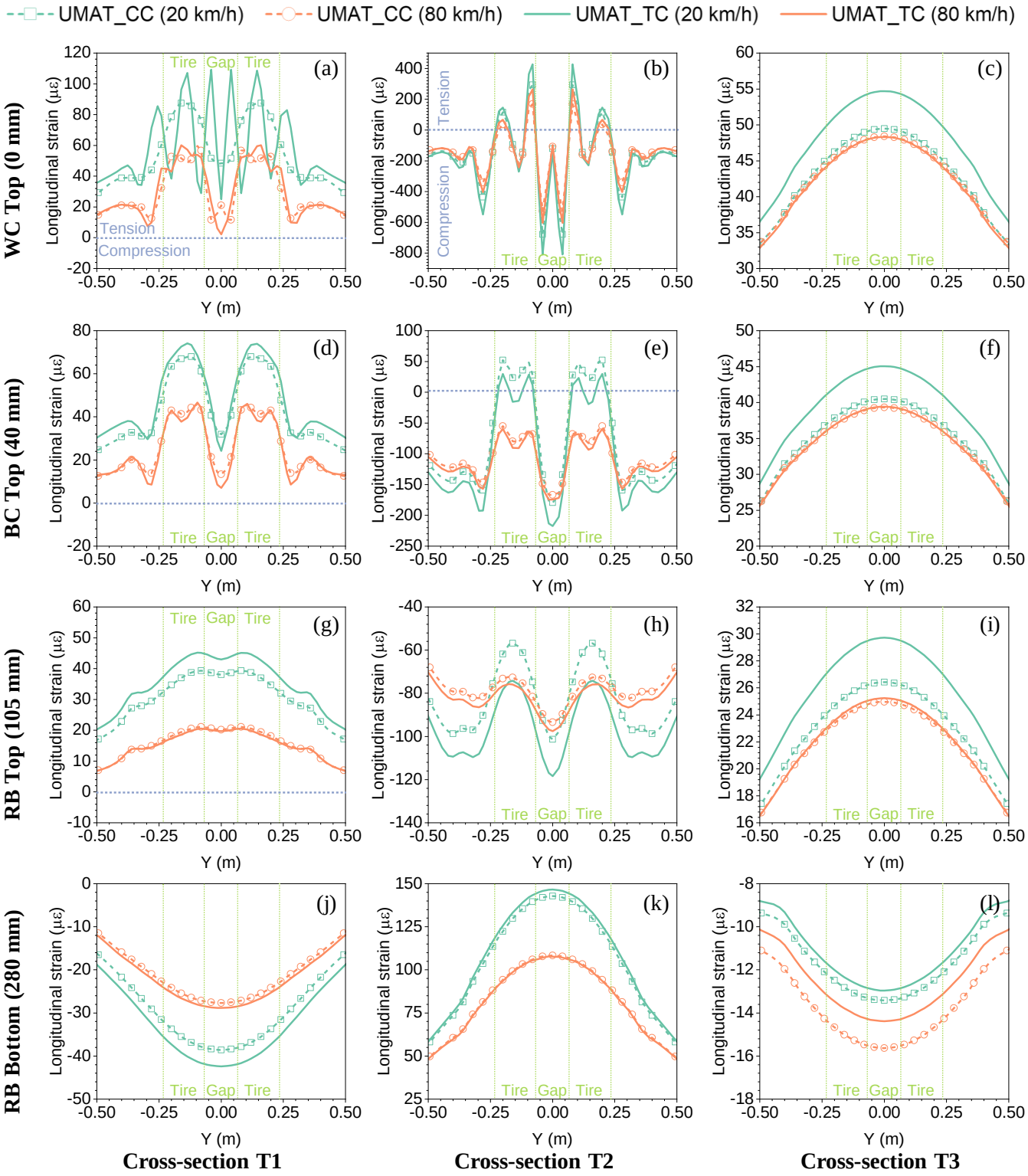

Figure 12 Longitudinal strains (E11)

6.3. Transverse strain (E22)

Figure 13 presents the distributions of the strain along the transverse direction (E22) in the pavement at 20 km/h. The transverse strain profile indicates a significant alternation of high tensile and compressive

strains beneath the dual-tire load, with higher tensile strains concentrated in the lateral regions of the tire load (orange color). Moreover, the exterior of the tire edges and the pavement's horizontal centerline exhibit higher tensile strain after wheel passing, indicating a notable influence of the dual-tire load on the transverse strains. Therefore, the transverse strains in the middle transverse cross-section (T2) and two longitudinal cross-sections: outside of the tire edge (L1), and the pavement's longitudinal centerline (L2), as shown in Figure 13(a), were further analyzed.

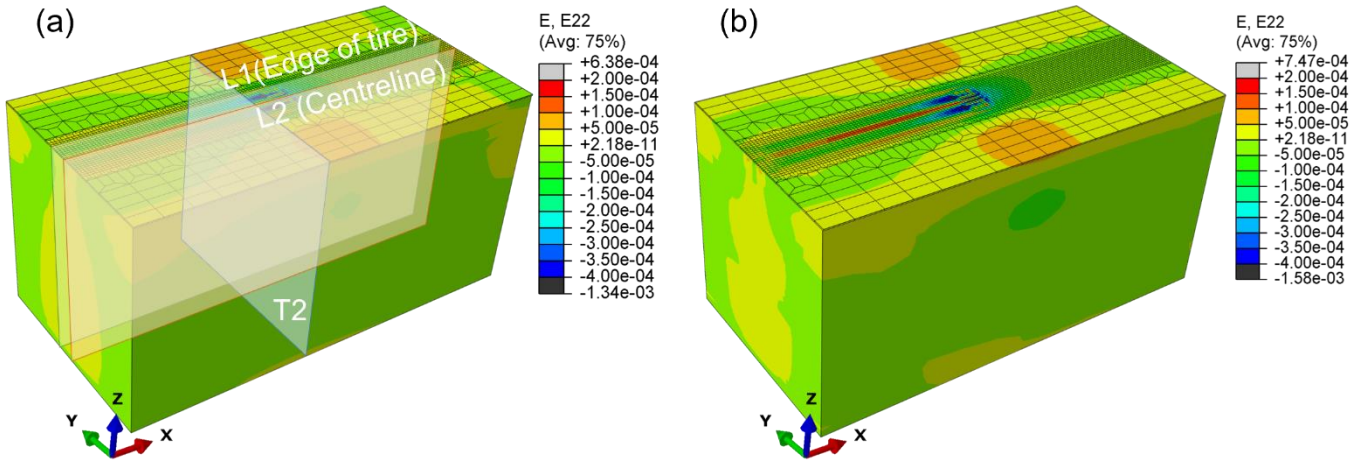

Figure 13 Transverse strains (E22) distributions at 20 km/h and 14:00 predicted by (a) UMAT_CC model; and (b) UMAT_TC model

Figure 14 presents the distributions of transverse strains in three selected cross-sections. From Figures 14(a), (d), (g) and (j), it can be found that, similar to the longitudinal tensile strain (E11), the UMAT_TC model primarily produces higher transverse tensile strains (E22) on the near surface of the pavement, which decrease with the increase in vehicular speed. Therefore, it is crucial to consider the tensile strain in the top AC layers during pavement design. However, the difference is that instead of the top surface of the WC layer, the pavement presents the maximum transverse tensile strain (E22) in the top surface of the BC layer (Figure 14(d)). Furthermore, AC's TC asymmetry leads to further increases in transverse strains. Under the tire load, the zones directly beneath exhibit maximum tensile strains of 497 με and 551 με for the UMAT_CC and UMAT_TC models, respectively, at a vehicular speed of 20 km/h (Figure 14(d)). This result signifies an 11% change in the predicted E22 by incorporating AC's TC asymmetry into the design and

analysis process, compared with the conventional pavement design method.

Regarding the transverse strains in the two longitudinal sections, it is interesting to note that a higher tensile strain still exists in the top AC layers in both longitudinal cross-sections after tire passing for the UMAT_TC model (Figure 14(b) and (c)). This response suggests that a longer recovery time may be necessary if AC's TC asymmetry is considered in the design process. Moreover, the clearance between the two tires also displays a maximum transverse tensile strain of around 400 με (Figure 14(c)). At a vehicular speed of 20 km/h, the maximum transverse tensile strains at the centerline of the pavement are 439 με and 489 με for the UMAT_CC and UMAT_TC models, respectively. This 12% increase in tensile strain may result in approximately 55% more damage to the asphalt pavement, according to the 4^{th} power law.

Therefore, it can be concluded that incorporating AC's TC asymmetry in the design process increases the transverse tensile strains primarily in zones beneath the dual-tire load and the clearance between dual tires, which may lead to longitudinal top-down cracking under repeated traffic loads. Therefore, it is crucial to consider AC's TC asymmetry in pavement design and analysis to improve its durability and longevity.

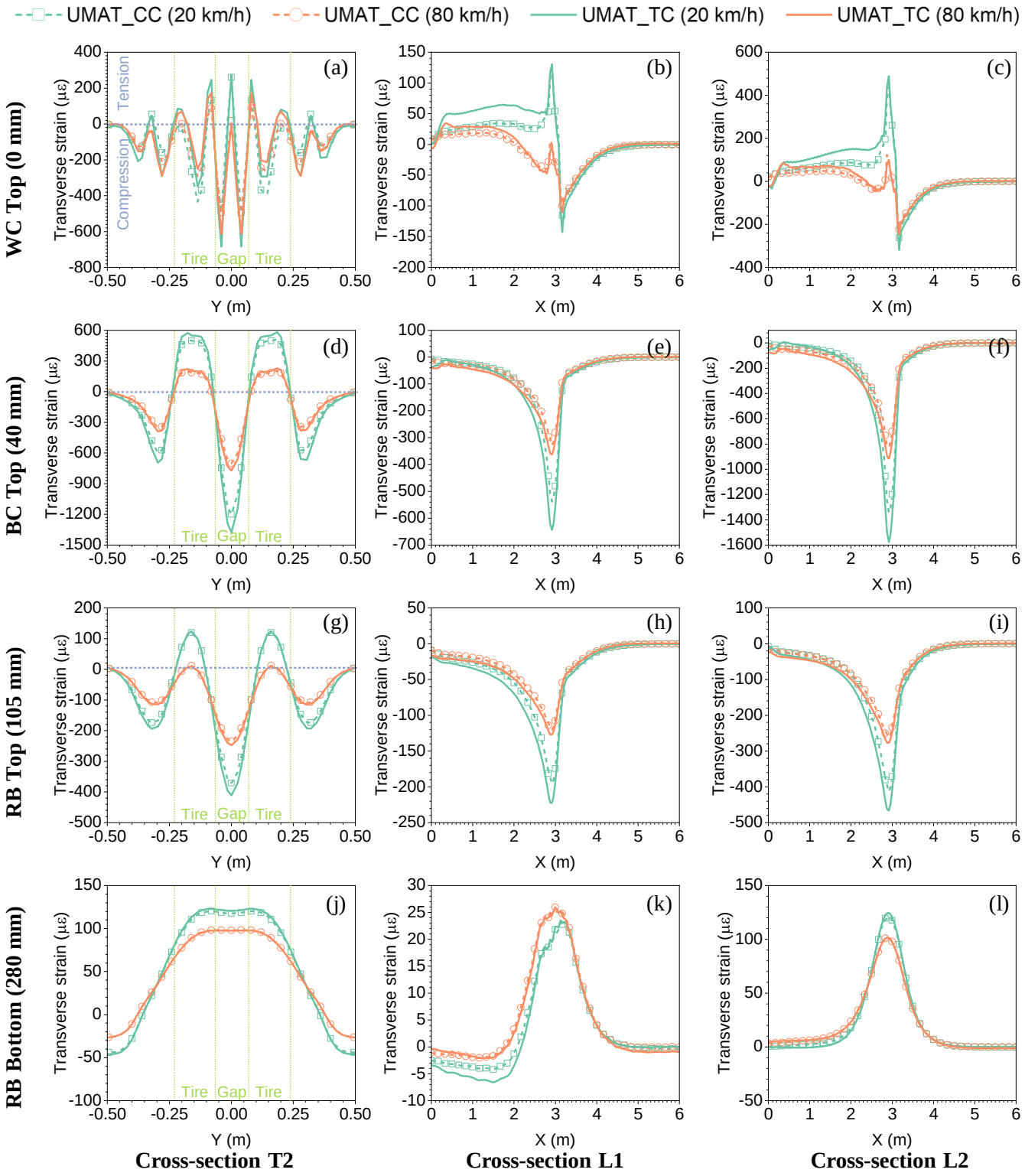

Figure 14 Transverse strains (E22)

6.4. Longitudinal shear strain (E13)

Figure 15 presents the longitudinal shear strain (E13) with pavement depths along the vertical centerline. Regardless of the vehicular speed, AC layers (WC, BC, and RB) exhibit high shear strains, with the maximum values found in the BC layer and decreasing in the RB layer. Incorporating TC asymmetry in the UMAT_TC model increases peak strains in the BC layer compared to the UMAT_CC model. This

increase is more pronounced under lower speed conditions (20 km/h). At the vehicular speed of 20 km/h, the maximum shear strains from the UMAT_CC and UMAT_TC models are 394 and 466 με, respectively. This indicates that considering AC asymmetry can lead to an 18% increase in longitudinal shear strain. It should be noted that higher shear strains can cause slippage of AC layers, which can lead to distresses such as shoving and debonding in the asphalt layers.

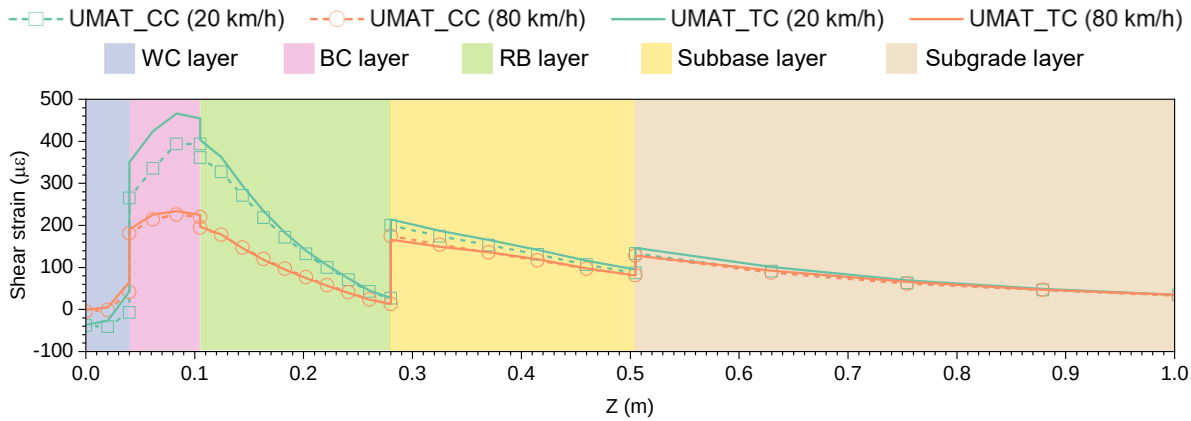

Figure 15 Shear strain (E13) along with the vertical centerline

6.5. Temperature effect

To evaluate the effect of temperatures, the pavement responses at the low temperature field (at 6:00) were also predicted. Figure 16 shows the predicted vertical deformation (U3), which significantly reduced compared to the deformation at 14:00 (Figure 9). At 20 km/h, the maximum deformation at 14:00 is approximately 0.7 mm, whereas at 6:00, it is no more than 0.28 mm. This reduction can be attributed to the lower temperatures at 6:00 (around 30 °C on the surface) compared to 14:00 (about 70 °C on the surface), making the AC mixtures stiffer and less asymmetric, resulting in lower vertical deformation in the AC layers. Figure 17 displays the vertical strain (E33) with pavement depth at 6:00, which reveals a significant reduction in maximum tensile and compressive vertical strains compared to those at 14:00. The lower temperature is equivalent to a higher frequency (vehicular speed), which can improve the modulus of AC mixtures and eventually help to reduce the impact of AC's TC asymmetry. Similar results were found for E11, E22, and E13. Therefore, it can be concluded that lower temperatures can alleviate the TC asymmetry of AC, resulting in lower tensile and shear strain in AC layers.

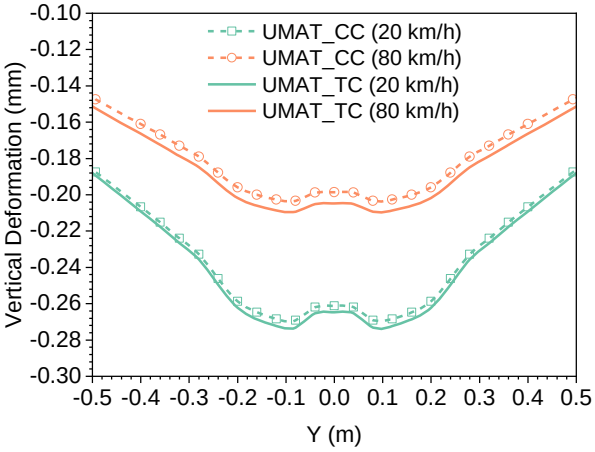

Figure 16 Predicted vertical deformation (U3) at low temperature field (at 6:00)

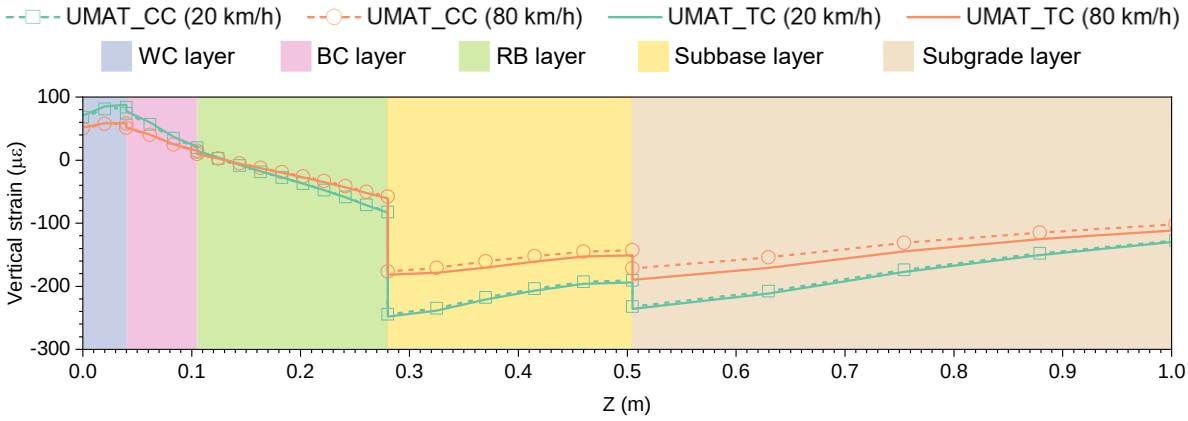

Figure 17 Vertical strain (E33) along the vertical centerline at low temperature field (at 6:00)

7. Findings and Conclusions

In this study, a temperature-dependent dual viscoelastic constitutive model was proposed to account for AC's TC asymmetry. Further, the corresponding UMAT subroutine was developed to introduce the AC's TC asymmetry to the numerical modeling of asphalt pavement. The main findings of this study can be summarized as follows:

- The proposed model effectively captured the asymmetric viscoelastic properties of AC in T&C and successfully introduced AC's asymmetry into the numerical modeling of asphalt pavements.
- Consideration of AC's TC asymmetry in the pavement model increased the vertical deformation and the vertical tensile strain at the interface between WC and BC layers due to the lower tensile modulus of AC.
- Contrary to conventional understanding, high tensile strains also exist in the top AC layers. For

pavement at the service temperature, consideration of TC asymmetry in the pavement modeling increased the maximum longitudinal and transverse tensile strains in the top AC layers by more than 30% and 10%, respectively, which may make the pavement more susceptible to top-down fatigue cracking under repeated traffic loads.

- AC's TC asymmetry increased the maximum shear strain in the BC layer, with an 18% increase observed at the high service temperature and low vehicular speed, which may cause shoving and debonding in AC layers.
- The influence of AC's asymmetry on pavement response was dependent on temperature and vehicular speed, with a higher degree of influence expected in regions experiencing lower vehicular speed or higher climatic temperature.

In conclusion, this study provides a comprehensive understanding of the asymmetric viscoelastic properties of AC and its influence on pavement performance. The developed UMAT subroutine presents an effective approach for introducing AC's TC asymmetry into the numerical simulation, which is expected give a more realistic prediction than the conventional simulation considering the compressive properties of AC only. The outcomes of this study can enhance the design and maintenance of durable asphalt pavements. It should be noted is that the result presented here is based on the typical pavement structure in Hong Kong. In future research, different pavement structures will be considered. Besides, stress and strain predictions derived from our pavement modeling will be employed in laboratory tests on AC samples. This approach will facilitate a comprehensive characterization of AC's performance under traffic loads, including its fatigue and rutting resistance. Furthermore, field tests will be conducted to validate the model proposed in this study.

Acknowledgments

The authors sincerely acknowledge the funding support from Hong Kong Research Grant Council through the GRF project 15220621.

Disclosure statement

No potential conflict of interest was reported by the authors.

References

Ahmed, M.U., Rahman, A., Islam, M.R., and Tarefder, R.A., 2015. Combined effect of asphalt concrete cross-anisotropy and temperature variation on pavement stress–strain under dynamic loading. *Construction and Building Materials*, 93, 685–694.

Alae, M., Leng, Z., Zhao, Y., and Fu, G., 2021. Viscoelastic analysis of surface responses in flexible pavements under different loading conditions. *Road Materials and Pavement Design*, 1–23.

Cai, X., Ashish, P.K., Leng, Z., Tan, Z., and Wang, H., 2024. Effects of residual water on mechanical properties of cold mix based semi-flexible pavement composite towards a sustainable paving material. *Journal of Cleaner Production*, 434, 139857.

Cai, X., Yang, J., Chen, X., Zhang, J., and Zhang, H., 2020. Interlocking property evaluation of dual skeleton in semi-flexible pavement material by micromechanical model and X-ray computed tomography. *Construction and Building Materials*, 254, 118934.

Cao, P., Jin, F., Zhou, C., and Feng, D., 2017. Investigation on statistical characteristics of asphalt concrete dynamic moduli with random aggregate distribution model. *Construction and Building Materials*, 148, 723–733.

Cao, P., Leng, Z., Shi, F., Zhou, C., Tan, Z., and Wang, Z., 2020. A novel visco-elastic damage model for asphalt concrete and its numerical implementation. *Construction and Building Materials*, 264, 120261.

Cheng, H., Wang, Y., Liu, L., Sun, L., Zhang, Y., and Yang, R., 2021. Estimating tensile and compressive moduli of asphalt mixture from indirect tensile and four-point bending tests. *Journal of Materials in Civil Engineering*, 33 (1), 04020402.

Cho, K.S., 2016. *Viscoelasticity of polymers*. Dordrecht: Springer Netherlands.

Dai, Z., Laheri, V., Zhu, X., and Gilabert, F.A., 2021. Experimental study of compression-tension asymmetry in asphalt matrix under quasi-static and dynamic loads via an integrated DMA-based approach. *Construction and Building Materials*, 283, 122725.

Darabi, M.K., Abu Al-Rub, R.K., Masad, E.A., Huang, C.-W., and Little, D.N., 2011. A thermo-viscoelastic–viscoplastic–viscodamage constitutive model for asphaltic materials. *International Journal of Solids and Structures*, 48 (1), 191–207.

Deng, Y., Luo, X., Gu, F., Zhang, Y., and Lytton, R.L., 2019. 3D simulation of deflection basin of pavements under high-speed moving loads. *Construction and Building Materials*, 226, 868–878.

Helmer-Smith, H., Vlachopoulos, N., Dagenais, M.-A., and Forbes, B., 2021. In-situ load testing of a WWII era timber Warren truss in the development of a structural health monitoring program. *Engineering Structures*, 239, 112274.

Huang, C.-Y., Stankiewicz, A., Ateshian, G.A., and Mow, V.C., 2005. Anisotropy, inhomogeneity, and tension–compression nonlinearity of human glenohumeral cartilage in finite deformation. *Journal of Biomechanics*, 38 (4), 799–809.

Jiang, X., Gabrielson, J., Titi, H., Huang, B., Bai, Y., Polaczyk, P., Hu, W., Zhang, M., and Xiao, R., 2022. Field investigation and numerical analysis of an inverted pavement system in Tennessee, USA. *Transportation Geotechnics*, 35, 100759.

Kallas, B.F., 1970. Dynamic modulus of asphalt concrete in tension and tension-compression. *In*: *Association of Asphalt Paving Technologists Proc*. 1–23.

Katicha, S.W., Flintsch, G.W., and Loulizi, A., 2010. Bimodular analysis of hot-mix asphalt. *Road Materials and Pavement Design*, 11 (4), 917–946.

Keshavarzi, B. and Kim, Y.R., 2016. A viscoelastic-based model for predicting the strength of asphalt concrete in direct tension. *Construction and Building Materials*, 122, 721–727.

Khanal, P. and Mamlouk, M., 1995. Tensile versus compressive moduli of asphalt concrete. *Transportation Research Record*, (1492), 144–150.

Lakes, R.S., 1998. *Viscoelastic solids*. CRC press.

Leng, Z., Tan, Z., Cao, P., and Zhang, Y., 2021. An efficient model for predicting the dynamic performance of fine aggregate matrix. *Computer-Aided Civil and Infrastructure Engineering*, 36 (11), 1467–1479.

Leng, Z., Tan, Z., Yu, H., and Guo, J., 2019. Improvement of storage stability of SBS-modified asphalt with nanoclay using a new mixing method. *Road Materials and Pavement Design*, 20 (7), 1601–1614.

Levenberg, E., 2015. Viscoelastic tension-compression nonlinearity in asphalt concrete. *Journal of Materials in Civil Engineering*, 27 (12), 04015048.

Li, H., Tan, Z., Li, R., Luo, X., Zhang, Y., and Leng, Z., 2024. Mechanistic modeling of fatigue crack growth in asphalt fine aggregate matrix under torsional shear cyclic load. *International Journal of Fatigue*, 178, 107999.

Lu, G., Törzs, T., Liu, P., Zhang, Z., Wang, D., Oeser, M., and Grabe, J., 2020. Dynamic response of fully permeable pavements: development of pore pressures under different modes of loading. *Journal of Materials in Civil Engineering*, 32 (7), 04020160.

Luo, X., Li, H., Deng, Y., and Zhang, Y., 2020. Energy-based kinetics approach for coupled viscoplasticity and viscofracture of asphalt mixtures. *Journal of Engineering Mechanics*, 146 (9), 04020100.

Lv, S., Liu, C., Yao, H., and Zheng, J., 2018. Comparisons of synchronous measurement methods on various moduli of asphalt mixtures. *Construction and Building Materials*, 158, 1035–1045.

Lytton, R.L., Gu, F., Zhang, Y., and Luo, X., 2018. Characteristics of undamaged asphalt mixtures in tension and compression. *International Journal of Pavement Engineering*, 19 (3), 192–204.

Mollica, F., Ventre, M., Sarracino, F., Ambrosio, L., and Nicolais, L., 2007. Implicit constitutive equations in the modeling of bimodular materials: An application to biomaterials. *Computers & Mathematics with Applications*, 53 (2), 209–218.

Monismith, C.L. and Secor, K.E., 1962. Viscoelastic behavior of asphalt concrete pavements. Presented at the International Conference on the Structural Design of Asphalt Pavements, Ann Arbor, Michigan, 728–760.

Nguyen, Q.T., Di Benedetto, H., Sauzéat, C., Nguyen, M.L., and Hoang, T.T.N., 2016. 3D complex modulus tests on bituminous mixture with sinusoidal loadings in tension and/or compression. *Materials and Structures*, 50 (1), 98.

Pan, Q., Zheng, C., Song, X., Lv, S., Yu, H., Zhang, J., Borges Cabrera, M., and Liu, H., 2021. Mechanical analysis of asphalt pavement based on bimodulus elasticity theory. *Construction and Building Materials*, 301, 124084.

Program (NCHRP), N.C.H.R., 2004. *Guide for mechanistic-empirical design of new and rehabilitated pavement structures*. Washington, DC: Transportation Research Board, No. National Cooperative Highway Research Program (NCHRP) Project 1-37A.

Sun, Y., Chen, J., Pan, B., Shu, X., and Huang, B., 2017. Three-dimensional micromechanical complex-modulus prediction of asphalt concrete considering the aggregate interlocking effect. *Journal of Materials in Civil Engineering*, 29 (10), 04017153.

Tan, Z., Guo, F., Leng, Z., Yang, Z., and Cao, P., 2024. A novel strategy for generating mesoscale asphalt concrete model with controllable aggregate morphology and packing structure. *Computers & Structures*, 296, 107315.

Tan, Z., Jelagin, D., Fadil, H., Leng, Z., Li, R., Jiang, J., and Cao, P., 2023. Virtual-specimen modeling of aggregate contact effects on asphalt concrete. *Construction and Building Materials*, 400, 132638.

Tan, Z., Leng, Z., Jelagin, D., Cao, P., Jiang, J., Kumar Ashish, P., and Zou, F., 2023. Numerical modeling of the mechanical response of asphalt concrete in tension and compression. *Mechanics of Materials*,

104823.
Tan, Z., Leng, Z., Jiang, J., Cao, P., Jelagin, D., Li, G., and Sreeram, A., 2022. Numerical study of the aggregate contact effect on the complex modulus of asphalt concrete. *Materials & Design*, 213, 110342.
Tan, Z., Yang, B., Leng, Z., Jelagin, D., Cao, P., Li, R., and Zou, F., 2023. Multiscale characterization and modeling of aggregate contact effects on asphalt concrete's tension–compression asymmetry. *Materials & Design*, 232, 112092.
Tschoegl, N.W., 1989. *The phenomenological theory of linear viscoelastic behavior*. Berlin, Heidelberg: Springer Berlin Heidelberg.
Zhang, H., Anupam, K., Scarpas, T., Kasbergen, C., and Erkens, S., 2021. Contact mechanics based solution to predict modulus of asphalt materials with high porosities. *Materials & Design*, 109752.
Zou, F., Leng, Z., Tan, Z., Li, D., Han, M., Lu, G., and Sreeram, A., 2024. Kinetics and toxicological potential of heavy metal leaching from asphalt pavements. *Science of The Total Environment*, 912, 169193.